The Gravity Wave–Arctic Stratospheric Vortex Interaction

THOMAS J. DUCK*

Department of Physics and Astronomy, York University, Toronto, Ontario, Canada

JAMES A. WHITEWAY

Department of Physics, University of Wales, Aberystwyth, United Kingdom

ALLAN I. CARSWELL

Department of Physics and Astronomy, York University, Toronto, Ontario, Canada

(Manuscript received 19 May 2000, in final form 16 April 2001)

ABSTRACT

Four hundred and twenty-two nights of stratospheric gravity wave observations were obtained with a Rayleigh lidar in the High Arctic at Eureka (80°N, 86°W) during six wintertime measurement campaigns between 1992/93 and 1997/98. The measurements are grouped in positions relative to the arctic stratospheric vortex for comparison. Low gravity wave activity is found in the vortex core, outside of the vortex altogether, and in the vortex jet before mid-December. High gravity wave activity is only found in the vortex jet after late December, and is related to strengthening of the jet and decreased critical-level filtering. Calculations suggest that the drag induced by the late-December gravity wave energy increases drives a warming already observed in the vortex core, thereby reducing vortex-jet wind speeds. The gravity waves provide a feedback mechanism that regulates the strength of the arctic stratospheric vortex.

1. Introduction

It is well known that the circulation of the middle atmosphere is strongly coupled to the troposphere by way of vertically propagating waves. This was first appreciated for the case of large-scale planetary waves, and a considerable body of literature that explores planetary wave–induced ''sudden stratospheric warming'' exists [see articles by Matsuno (1971), Palmer (1981), McIntyre and Palmer (1983, 1984), and Fairlie and O'Neill (1988), and reviews by Labitzke (1981) and Schoeberl (1978)]. With the advent of lidars and advances in other instrumentation, small-scale internal gravity waves have received an increased amount of observational attention. Gravity wave momentum deposition in the mesosphere is already recognized to drive the reversed mesospheric meridional temperature gradient (Lindzen 1981; Matsuno 1982; Holton 1983); however, the degree to which gravity waves affect the large-scale thermal structure of the stratosphere is a matter of continued debate.

Observational evidence for gravity wave–induced stratospheric warming was found by Duck et al. (1998) in measurements of temperatures and gravity wave energies obtained with a lidar in the High Arctic at Eureka (80°N, 86°W). By grouping the measurements in positions relative to the arctic stratospheric vortex, they identified an annual warming in the vortex core's upper stratosphere and recognized that it was correlated with increased gravity wave activity in the vortex jet. It was proposed that the warming was forced by a gravity wave–induced circulation, that is, the same mechanism used to explain the reversed mesospheric meridional temperature gradient.

Although stratospheric warming is most often attributed to the effects of planetary wave breaking, there are precedents that show gravity wave drag can significantly impact temperatures in the stratosphere. For example, Holton's (1983) zonal-mean circulation model, with no planetary wave parameterization and the gravity wave drag tuned to ensure a realistic mesosphere, produced realistically warm temperatures in the polar upper stratosphere, a structure that Hitchman et al. (1989) termed the ''separated polar stratopause.'' Kanzawa (1989) has pointed out that the wintertime stratopause over Antarctica is significantly warmer than that over the Arctic even though there is much less planetary

* Current affiliation: Department of Physics, Dalhousie University, Halifax, Nova Scotia, Canada.

Corresponding author address: Thomas J. Duck, Dept. of Physics, Dalhousie University, Halifax, NS B3H 3J5, Canada.

wave activity in the Southern Hemisphere; this implies that a contributor of drag in addition to planetary wave breaking is important to stratospheric dynamics.

In this study the gravity wave observations obtained with the lidar at Eureka are examined in detail. Data from the 1992/93–1997/98 wintertime campaigns are used, forming a large sample of 422 nights of observation. Using a statistical approach, the late-December gravity wave activity increases are highlighted. Building upon the results of Whiteway et al. (1997), the statistical relationships between gravity wave energies, wind speeds, and critical-level filtering are established. Changes in the statistics of vortex-jet wind speeds and critical-level filtering are used to provide an explanation for the late-December gravity wave activity rise. Finally, a calculation based upon the transformed Eulerian mean (TEM) circulation equations (Andrews and McIntyre 1976; Palmer 1981) is used to demonstrate that the late-December increases in gravity wave activity may drive a warming in the upper stratosphere of the vortex core, thereby reducing the vortex-jet wind speeds. The measurements and calculation imply that gravity waves provide a feedback mechanism that regulates the strength of the arctic stratospheric vortex.

2. Instrumentation and data analysis

a. Rayleigh lidar observations of gravity wave activity

The measurements presented here were obtained with a lidar (laser radar) based in the High Arctic at Eureka (80°N, 86°W) during the winters of 1992/93–1997/98. Technical details regarding the lidar are given by Carswell et al. (1993) and Duck (1999), and an operational description is provided by Duck et al. (2000a). Gravity waves are observed as perturbations in 10-min average temperature profiles obtained using the Rayleigh lidar technique (Hauchecorne and Chanin 1980). Figure 1 gives an example of a perturbed temperature profile, and additional case studies are presented by Whiteway and Carswell (1994) and Whiteway et al. (1997).

The night-mean perturbation potential energy density is used to gauge the gravity wave activity for each night. The perturbation potential energy per unit mass E_p is given by

$$E_p = \frac{1}{2}\left(\frac{g}{N}\right)^2 \overline{\left(\frac{T'}{T_0}\right)^2},$$

where g is the gravitational acceleration, N is the buoyancy frequency, and $\overline{(T'/T_0)^2}$ is the mean fractional temperature variance. The procedure employed to extract the gravity wave perturbations and used to determine the perturbation potential energy is explained in the appendix; it is shown that gravity wave energies are reliably measured for vertical wavelengths between 2 and 15 km.

An average of 26 ($\pm$10) perturbation profiles are obtained in a night of observations. The duration of measurements for any given night is determined mostly by the observing conditions (measurements cannot be obtained when there is cloud cover). All of the profiles collected in a night of measurements are used to determine the night-mean perturbation potential energy profile, which typically extends from 30 to 45 km in altitude. The measurements presented here are mostly averages from the 30–35-km altitude range, and similar results are obtained from the 35–40- and 40–45-km ranges unless noted otherwise.

b. Influence of background winds on wave propagation

The capacity for gravity waves to propagate from tropospheric sources into the stratosphere is largely determined by the intervening background winds. In the analysis that follows, the gravity wave energy measurements are related to simple propagation indices based upon background wind profiles in order to identify the most important statistical relationships.

Consider first that gravity waves with frequencies kc are Doppler shifted to intrinsic frequencies ω given by

$$\omega = k(c - U\cos\theta), \tag{1}$$

where c is the gravity wave's horizontal phase speed and $\theta(z)$ is the angle between the gravity wave's horizontal wavevector $\mathbf{k}$ and the background wind $\mathbf{U}(z)$. For waves of intermediate frequencies, $N \gg \omega \gg f$ (where f is the Coriolis parameter), the gravity wave dispersion relation reduces to

$$\lambda_z \equiv \frac{2\pi}{m} \approx \frac{2\pi}{N}\frac{\omega}{k} = \frac{2\pi}{N}(c - U\cos\theta), \tag{2}$$

where λ_z is the vertical wavelength and m is the vertical wavenumber. The dispersion relation shows that Doppler shifting to small vertical wavelengths occurs whenever $U(z)\cos\theta(z)$ approaches c, which gives rise to instabilities and turbulent dissipation. The obstruction of gravity waves in this way is referred to as critical-level filtering and is discussed in detail by Bretherton (1966) and Booker and Bretherton (1967). A source spectrum of upward-propagating gravity waves will be assumed and the amount of gravity wave transmission into the stratosphere will be determined by identifying critical levels.

The lidar measurements at Eureka contain no direct information on gravity wave horizontal phase speeds or directions, so some approximations must be made in this regard. First, since there is surely little convective gravity wave generation during the dark months of the high arctic winter, orographic generation (where $c = 0$ in the steady state) is likely the dominant contributor to the gravity wave field. This assumption is supported by observations at Eureka during winter that often show stationary or very slowly progressing waves (Whiteway and Carswell 1994). Because the midlatitude jet stream rarely reaches the high Arctic (see, e.g., Whiteway and

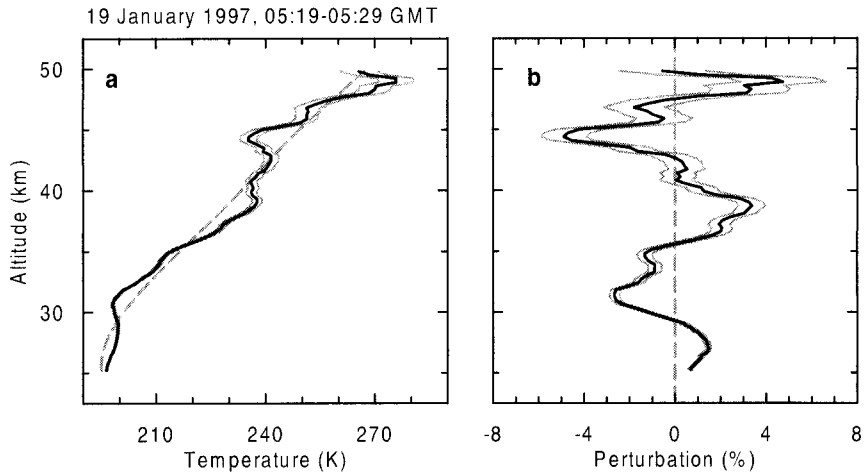

FIG. 1. (a) A 10-min average temperature measurement obtained on 19 Jan 1997. The solid line is the temperature profile and the gray lines indicate the measurement uncertainties. The background profile given by the dashed line was fitted to the temperature profile according to the procedure outlined in the appendix; (b) the corresponding perturbation profile.

Duck 1999), the contribution to the gravity wave field from jet and shear sources is expected to be small. Moreover, a high-resolution modeling of nonorographic waves by Sato et al. (1999) shows little gravity wave activity in the Arctic compared to lower latitudes.

Second, we will assume that many gravity waves are excited at any given time with horizontal wave vectors in a variety of directions. Horizonal wave vectors for waves generated by ridgelike features are oriented perpendicular to the long axis of the topography (Hines 1988). Because mesoscale ridges in the upstream vicinity of Eureka are oriented in a variety of directions (Bacmeister 1993), the azimuthal distribution of horizontal wave vectors should be roughly semicircular and away from the source level wind direction; for example, if the source level wind is directed eastward then the horizontal wave vectors will be directed in the half-circle sweeping from north to south through west. Measurements in the Arctic by Yoshiki and Sato (2000) suggest that this choice of source spectrum is indeed realistic. Equivalently for the transmission calculations that follow, the azimuthal distribution of horizontal wave vectors can be taken as isotropic.

For gravity waves with $c = 0$, Eq. (2) shows that critical-level filtering occurs when either $U = 0$ or $\theta = \pm 90°$. If the background wind turns between the source and measurement altitudes, a range of propagation directions is prohibited. Following Dunkerton and Butchart (1984), this can be used to define an average transmission $\overline{\tau}$ for waves propagating between altitudes z_1 and z_2. For horizontal wave vectors directed at angles α from $\mathbf{U}(z_1)$, the average transmission for a semicircular (or isotropic) azimuthal source spectrum of zero phase speed waves is given by

$$\overline{\tau} = \frac{1}{\pi} \int_{-\pi/2}^{\pi/2} \tau[\theta(\alpha, z)]\, d\alpha, \tag{3}$$

where

$$\tau[\theta(\alpha, z)] = \begin{cases} 0, & \text{if } \theta(\alpha, z) = \pm 90° \quad \text{at any altitude } z_1 < z < z_2, \\ 1, & \text{otherwise.} \end{cases}$$

This is essentially the same scheme explained with diagrams by Whiteway and Duck (1996), except that here the amount of wind turning is expressed as an equivalent transmission.

The average transmission for orographic waves was calculated for every day from November through March of 1992/93–1997/98 by using the geostrophic winds above Eureka derived from National Centers for Environmental Prediction (NCEP) constant-pressure height analyses; see Duck et al. (2000a) for details regarding the treatment of NCEP analysis products as used here. The geostrophic winds are generally in good agreement with the radiosonde measurements made at Eureka (Duck 1999). Significant differences in the wind direction only occur when the wind speeds are very low (i.e., <4 m s^{-1}). Winds derived from the NCEP analyses were used for the transmission calculations rather than radiosonde measurements because the analyses are considered to be more representative of the large-scale background conditions.

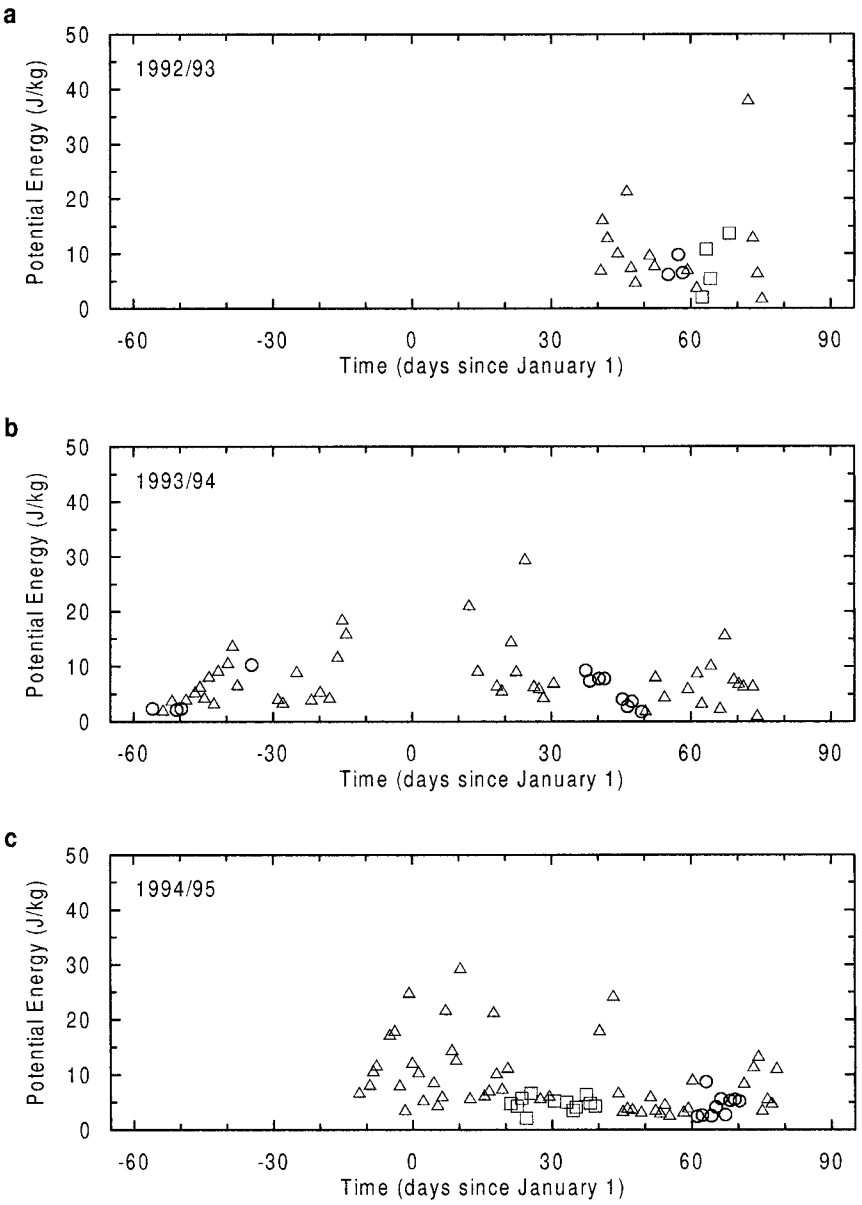

FIG. 2. Gravity wave potential energy densities measured during the winters of 1992/93–1997/98 by the lidar at Eureka (nightly averages for 30–35 km in altitude). The measurements are marked according to where they were obtained with respect to the vortex as follows: ○ = vortex core, △ = vortex jet, □ = outside of the vortex altogether.

The NCEP analyses are also used to group the gravity wave energy measurements in positions relative to the stratospheric vortex; that is, in the vortex core, within its cyclonic jet, and outside of the vortex altogether. In a presentation of night-averaged temperatures corresponding to the gravity wave observations examined here, Duck et al. (2000a) defined each region by measuring the position of Eureka relative to the vortex axis and vortex-jet wind speed maximum. Their classification scheme has been adopted for consistency, noting that a measure of the vortex position based upon winds was used in anticipation that gravity waves are modulated by the background winds through which they propagate.

3. Observations

a. Night-mean measurements of gravity wave activity

Figure 2 gives the measurements of gravity wave potential energy density obtained in the 30–35-km altitude range during each wintertime measurement campaign at Eureka between 1992/93 and 1997/98. As is shown in

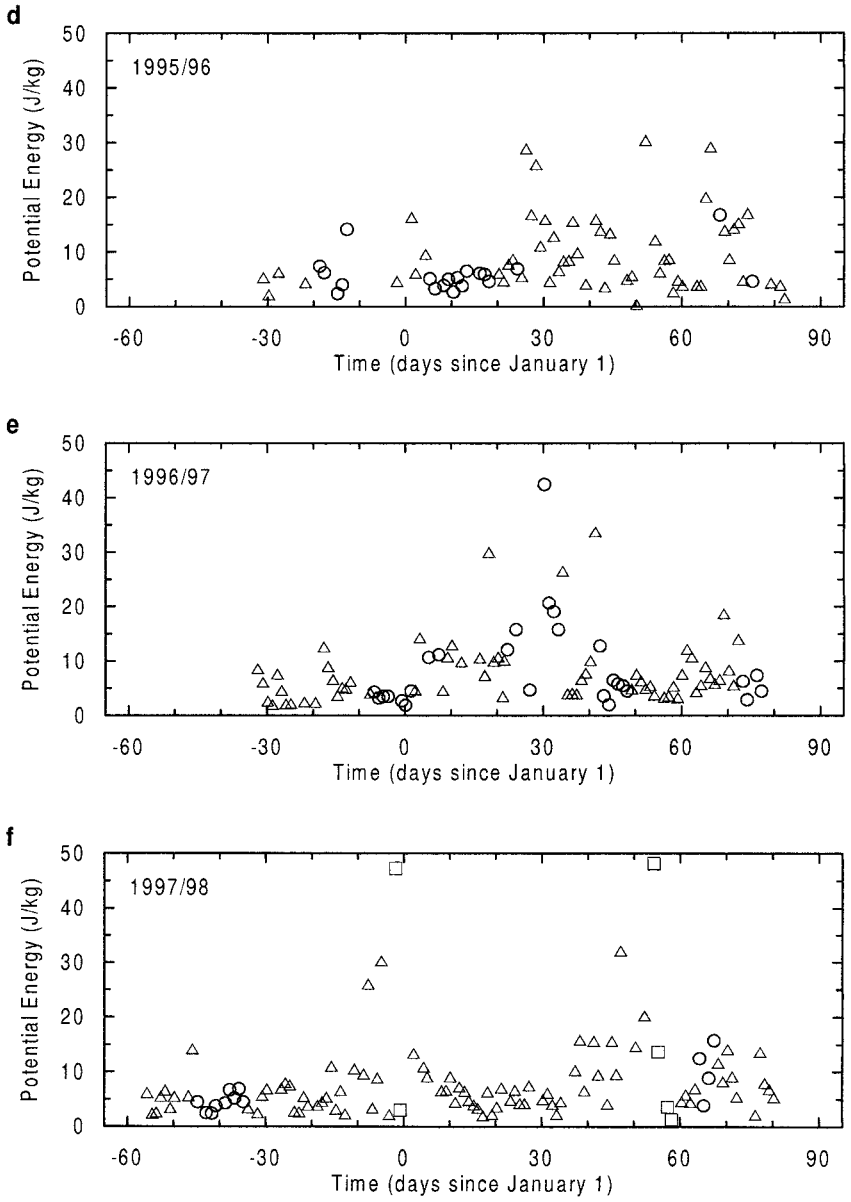

FIG. 2. (*Continued*)

Fig. 2, the observed gravity wave activity was highly variable. Where there was some consistency in the large-scale stratospheric thermal structure each night (Duck et al. 2000a), the gravity wave energy densities often changed dramatically.

Further examination of Fig. 2 shows that gravity wave energies obtained in the vortex core and outside of the vortex altogether were generally low (a point that will be verified statistically in what follows). In the vortex jet, episodes of high gravity wave activity were evident in addition to some lower values. Moreover, the episodes of high gravity wave activity were only observed at times later than mid-December. To illustrate this point more clearly, a scatterplot showing all of the gravity wave measurements obtained in the vortex jet, with 1 January of each year taken as day zero, is given in Fig. 3.

Figure 3 reveals that during November and much of December, the gravity wave energies within the vortex jet were relatively low; however, in mid- to late December episodes of high gravity wave activity were apparent and were observed through the end of measurements in late March. In what follows, measurements in the vortex jet will be separated into two different time periods: those obtained before mid-December and those taken in late December or thereafter. No such divisions in time will be made for measurements taken in the vortex core or outside of the vortex altogether since the gravity wave potential energies seen there were gen-

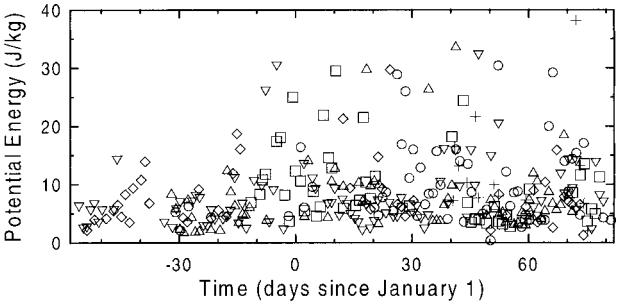

FIG. 3. The wintertime evolution of gravity wave potential energy density measurements (30–35 km) in the vortex jet. Symbols correspond to measurements during a particular winter: + = 1992/93, ◇ = 1993/94, □ = 1994/95, ○ = 1995/96, △ = 1996/97, ∇ = 1997/98.

erally low, and also because the quantity of data obtained in those regions before mid-December does not allow for a good statistical analysis.

Table 1 lists the average and standard deviation for the gravity wave energy distributions measured in each vortex region (and for different time periods, where applicable). In the vortex core the gravity wave energies were generally low. In the vortex jet the average gravity wave energy was low during November to mid-December and increased by 59 ± 14% for measurements taken after late December, a change that is separated by eight standard deviations of the mean. The standard deviation of the distribution taken after late December is much larger than for before mid-December, which reflects that the gravity wave energies were spread to higher values at that time. Outside of the vortex altogether, the average gravity wave energy appears to have been high, but the large standard deviation of the mean reflects the fact that a few outliers significantly affected the statistics there. A more appropriate way to compare changes in the gravity wave field when this is the case is to view probability density histograms.

Figure 4a presents histograms for measurements obtained in the vortex core and for measurements obtained in the vortex jet after late December. The use of histograms removes biases that might occur when viewing scatterplots (such as the ones in Figs. 2 and 3) by eye due to uneven data density. As is shown in Fig. 4a, the distribution of energies for measurements obtained in the vortex core is markedly different from the distribution for measurements taken in the vortex jet after late December. The vortex core distribution is sharply peaked near 4 J kg^{-1}, whereas the vortex jet distribution is broadly peaked near 4 or 5 J kg^{-1} and is spread so that higher energy values have a significant occurrence probability. Although the displacement between maximums is small, the sharpness of the vortex core peak ensures that many more of the measurements there have energies less than 6.5 J kg^{-1} than for measurements in the vortex jet. Note that small variations seen in the distributions of Fig. 4a (such as the local minimum at 4 J kg^{-1} in the vortex core profile) are not considered significant.

TABLE 1. Gravity wave potential energy distribution statistics for the vortex core, vortex jet (separately for dates earlier than 17 Dec and later than 26 Dec) and outside of the vortex altogether. The number of measured profiles (N_P), the average potential energy in the 30–35-km altitude ($\langle E_p \rangle$), and the standard deviation of the distribution (σ) are given for each region.

Region	N_P	$\langle E_p \rangle$ (J kg^{-1})	σ (J kg^{-1})
Vortex core	84	6.7 ± 0.62	5.7
Vortex jet ($t <$ Dec 17)	61	5.9 ± 0.44	3.4
Vortex jet ($t >$ Dec 26)	235	9.4 ± 0.44	6.8
Outside of vortex	22	9.4 ± 2.7	12.8

Figure 4b shows accumulated probability distributions for the gravity wave energy distribution observed in each vortex region (and time periods, where applicable). For a distribution across any variable x with probability densities $\psi(x)$, the accumulated (or integrated) probability $P(x \leq a)$ is given by

$$P(x \leq a) = \int_{-\infty}^{a} \psi(x)\, dx.$$

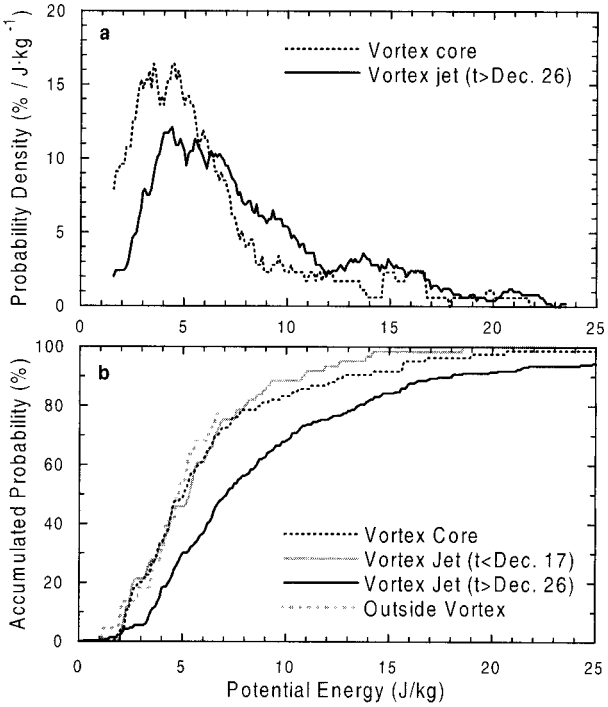

FIG. 4. (a) Gravity wave potential energy histograms for measurements at Eureka in the 30–35-km altitude range, each smoothed with a 2 J kg^{-1} boxcar mean. Calculations were performed separately for observations in the vortex core, in the vortex jet (before 17 Dec and after 26 Dec separately), and outside the vortex altogether, although only two histograms are shown in (a) for clarity. (b) Accumulated probability distributions for the measurements of gravity wave potential energy density in each vortex region. The distribution for outside the vortex is stopped where the data become too sparse to produce a meaningful curve.

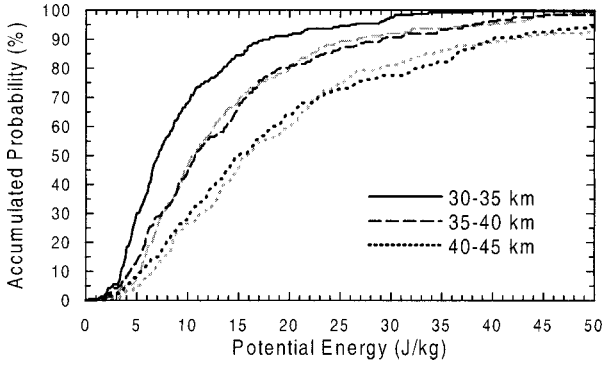

FIG. 5. Accumulated probability distributions for measurements of gravity wave potential energy density in the vortex jet after 26 Dec for three different altitude ranges. Predicted distributions based on energy conservation requirements (exponential growth from the next lower level) are given in gray.

For these observations, the accumulated probability is simply the fraction of measurements that yield energy values E_p less than a chosen gravity wave potential energy value E_0, that is, $P(E_p \leq E_0)$. Graphs of accumulated probability present the same information as histograms, except that the considerable smoothing (or ''binning'') required to produce histograms for continuous data is not required. Furthermore, distributions that are similar in nature may be more easily identified by using the accumulated probability.

As is shown in Fig. 4b, the distributions for gravity wave potential energy densities obtained in the vortex core, within the jet before mid-December, and outside of the vortex altogether are very similar for a broad range of energy values. This suggests that the conditions regulating the gravity wave propagation for those cases were similar, a fact that will be demonstrated. For measurements obtained in the vortex jet after late December, the accumulated probability distribution is different from the others, and it will be shown that this was due to changed propagation conditions.

Figure 5 shows accumulated probability distributions for the gravity wave energy measurements obtained in the vortex jet after late December for three different altitude ranges. Figure 5 illustrates that there is a shift with increasing altitude to gravity waves with higher potential energy densities, and that the shift is quantitatively consistent with energy conservation for gravity waves in a shearless flow. The energy conserving predictions were determined for each night of measurements at each altitude by multiplying the gravity wave energy of the underlying level by a factor of $\exp[5\text{ km}/(2RT_{\text{av}}g^{-1})]$, where R is the gas constant, T_{av} is the mean temperature of the two levels, and g is the gravitational acceleration. Measurements obtained in the vortex core, in the jet before late December and outside of the vortex altogether reveal growth with height but at a rate somewhat slower than conservative (not shown).

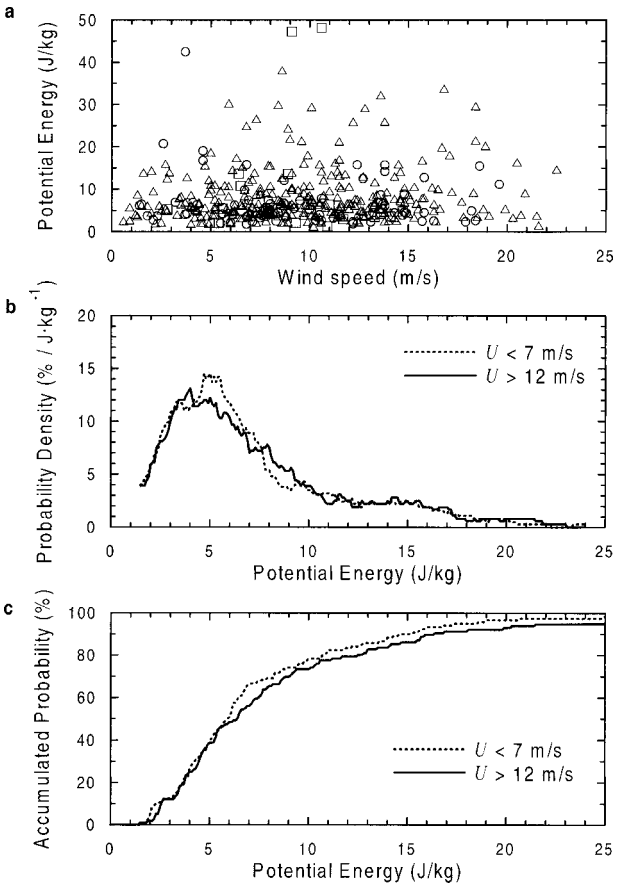

FIG. 6. (a) A scatterplot of gravity wave potential energy densities (30–35 km) vs the wind speed at 5 km in altitude. The measurements are marked according to where they were obtained with respect to the vortex as follows: ○ = vortex core, △ = vortex jet, □ = outside of the vortex altogether. (b) Gravity wave potential energy histograms for measurements in different wind speed ranges (U), each smoothed with a 2 J kg^{-1} boxcar mean (c) The corresponding (unsmoothed) graphs of accumulated probability for the histograms given in (b).

b. Statistical relationship between gravity waves and background wind speeds

1) TROPOSPHERIC WINDS

Figure 6a shows the gravity wave potential energy density measurements as a function of the wind speed at the 5-km height level. Radiosonde observations at Eureka have shown a strong connection between gravity wave energies in the lower stratosphere and low-level wind speeds (Whiteway and Duck 1996). However, no such relationship is apparent in the measurements of Fig. 6a. To ensure that the eye is not fooled by variations in the data density, histograms and accumulated probability distributions for measurements in different wind speed regimes are given in Figs. 6b and 6c, respectively. Figures 6b and 6c confirm that gravity wave energies in the middle stratosphere are only marginally higher for strong tropospheric wind speeds. Note that similar results are obtained when the winds at lower levels are

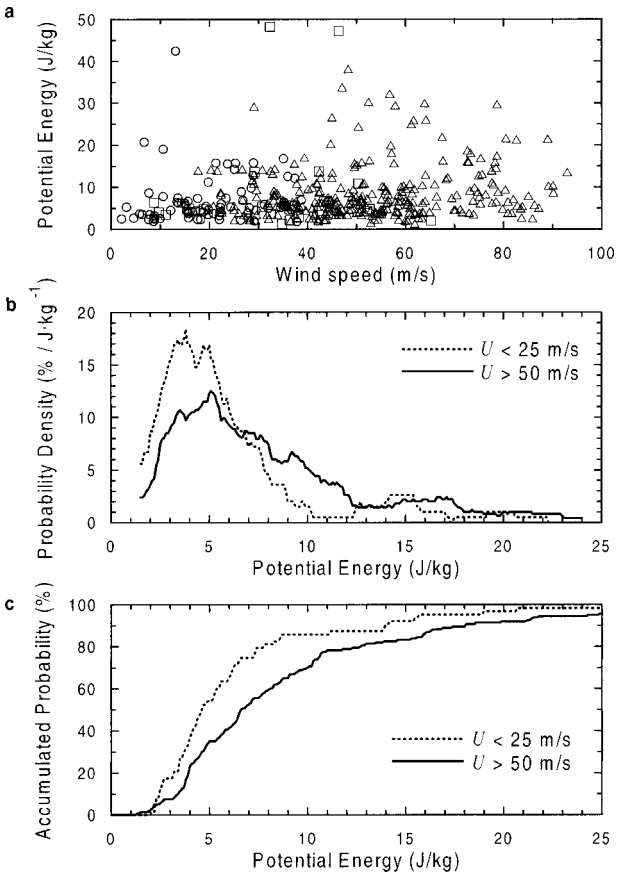

FIG. 7. (a) A scatterplot of gravity wave potential energy densities (30–35 km) vs the wind speed at 30 km in altitude. The measurements are marked according to where they were obtained with respect to the vortex as follows: ○ = vortex core, △ = vortex jet, □ = outside of the vortex altogether. (b) Gravity wave potential energy histograms for measurements in different wind speed ranges (U), each smoothed with a 2 J kg^{-1} boxcar mean. (c) The corresponding (unsmoothed) graphs of accumulated probability for the histograms given in (b).

used; we have used the midtropospheric values because they span a wider range of speeds and thus provide more certainty when the distributions are constructed.

Since the tropospheric wind speed is usually taken as the forcing strength for orographic gravity waves, it is at first surprising that a strong relationship is not apparent in Fig. 6. However, this result is consistent with measurements in the Arctic by Yoshiki and Sato (2000), who found a strong correlation between the gravity wave activity at lower altitudes and the source level winds but only a weak correlation for gravity wave energies obtained near our measurement range. We will show for our higher altitude measurements that the propagation conditions are of greater importance than the source level forcing strength.

2) STRATOSPHERIC WINDS

Figure 7a shows the gravity wave potential energy density measurements as a function of the wind speed

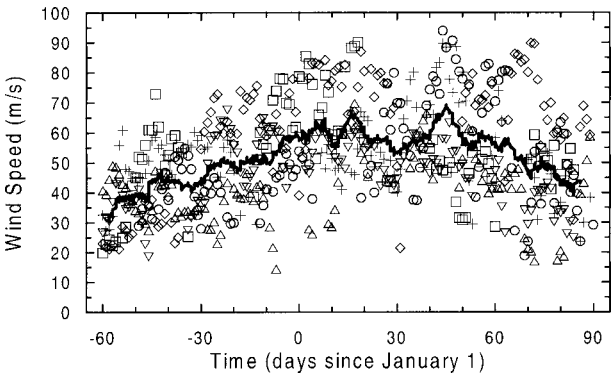

FIG. 8. A scatterplot of the wind speed in the vortex jet at the 30-km altitude level, sampled above Eureka from NCEP analyses for each season from 1992/93 to 1997/98. Symbols correspond to data from particular winters: + = 1992/93, ◇ = 1993/94, □ = 1994/95, ○ = 1995/96, △ = 1996/97, ∇ = 1997/98. The solid line represents a 21-point running mean.

at 30 km in height. As is shown in Fig. 7a, the majority of gravity wave measurements obtained when the stratospheric wind speeds were low gave low energy densities. For high stratospheric winds, the distribution of gravity wave energies is spread to much higher values. Histograms and accumulated probability distributions for measurements in different wind speed regimes are given in Figs. 7b and 7c, respectively. For stratospheric wind speeds less than 25 m s^{-1}, the histogram of gravity wave energies is sharply peaked near 4 J kg^{-1}. For stratospheric wind speeds greater than 50 m s^{-1}, the distribution of gravity wave energies is broad and peaked somewhere between 4 and 5 J kg^{-1} (note again that small variations seen in the distributions of Fig. 7b are not considered significant). Although the displacement between maximums is small, the sharpness of the peak for low stratospheric wind speeds ensures many more measurements there with energies less than 6.5 J kg^{-1} than when the stratospheric wind speeds are high. This is reinforced by the accumulated probability distributions given in Fig. 7c, which show that for any given gravity wave potential energy value, there are more measurements in high winds with energies greater than a chosen value than there are for low wind speeds.

Whiteway et al. (1997) provided an explanation for why the highest gravity wave energies are found in the vortex jet. They showed that elevated levels of gravity wave activity above Eureka correspond to an enhancement in the long vertical wavelength portion of the gravity wave spectrum. Equation (2) indicates that gravity waves are Doppler shifted to these long vertical wavelengths by the high wind speeds found in the vortex jet.

Because vortex-jet gravity wave energies were observed to increase in late December (shown in Fig. 3), it is of interest to know how the winds evolved during that time. A scatterplot of wind speeds at the 30-km altitude level for every day that the vortex jet was over Eureka during November through March of 1992/93–1997/98 is given in Fig. 8. As is shown in Fig. 8, the

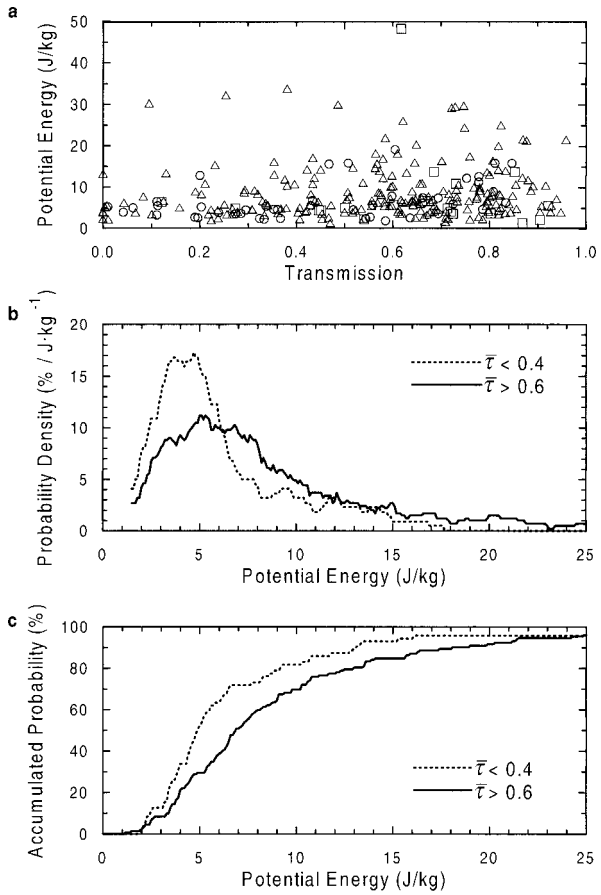

FIG. 9. (a) A scatterplot of gravity wave potential energy densities (30–35 km) vs the gravity wave transmission for steady orographic waves calculated between heights of 5 and 30 km. The measurements are marked according to where they were obtained with respect to the vortex as follows: ○ = vortex core, △ = vortex jet, □ = outside of the vortex altogether. (b) Gravity wave potential energy histograms for two different transmission ranges ($\overline{\tau}$), each smoothed with a 3 J kg^{-1} boxcar mean. (c) The corresponding (unsmoothed) graphs of accumulated probability for the histograms given in (b).

stratospheric vortex jet typically strengthened during November and much of December, and then leveled off. From the relationship already established between wind speeds and gravity wave energies, it follows that the evolution of the stratospheric vortex contributed to the observed increases in gravity wave activity.

c. Statistical relationship between gravity wave activity and critical-level filtering

Figure 9 shows the measured gravity wave potential energy densities as a function of the average gravity wave transmission index. The gravity wave transmission was calculated between $z_1 = 5$ and $z_2 = 30$ km for each day from wind profiles taken from the NCEP analyses. The two levels correspond to midtropospheric and midstratospheric levels, respectively. Only days when the winds exceeded 4 m s^{-1} between z_1 and z_2 are considered, because the direction for wind speeds less than that value are uncertain. This also loosens the restriction regarding gravity wave phase speeds: many waves with phase speeds less than 4 m s^{-1} are removed by a turning of the background wind. Approximately one-third of the measurements were excluded by using these criteria. Lowering z_1 disallows an increasing number of measurements because wind speeds decrease rapidly toward the ground.

As is shown in Fig. 9a, the gravity wave potential energy densities for low transmission values are generally small. For increased transmission, the gravity wave potential energy distribution is spread to higher values. Note that when the transmission is high, a broad range of gravity wave energies is still expected because of the variable source strength at lower levels.

Figures 9b and 9c give gravity wave energy histograms and accumulated probability distributions, respectively, for two different transmission ranges. As can be seen in Fig. 9b, for low transmission, the distribution is sharply peaked at low energies, whereas for high transmission the gravity wave energies are spread to higher values.

Similar to the analysis for winds, the wintertime evolution of critical-level filtering may be examined. For this calculation, no restrictions on wind speed were used in order to avoid biasing the results toward high values of transmission. The restrictions were previously necessary because one measured variable (gravity wave energy) was being compared to another (gravity wave transmission).

Histograms for transmission values in the vortex core and vortex jet are given in Fig. 10. As is shown in Fig. 10a, the histogram of gravity wave transmission in the vortex jet before mid-December essentially formed a white noise spectrum; that is, there were approximately equal probabilities for both high and low transmission values. This contrasts with the transmission distribution taken after late December, which is peaked at high values. After late December there was less potential for critical-level filtering in the vortex jet than before mid-December, which is consistent with the observed late-December increase in gravity wave activity.

Figure 10b shows that the accumulated probability distributions for measurements obtained in the vortex core and vortex jet before mid-December are very similar in form. The offset seen between the two is due to the fact that there are more occasions of 100% critical-level filtering in the vortex core than in the vortex jet before mid-December. That propagation conditions for gravity waves in the vortex jet before mid-December and in the vortex core were similar provides an explanation for the nearly identical energy distributions that were shown for those regions in Fig. 4b.

4. The gravity wave–induced circulation

The observations presented in section 3 show a late-December increase in vortex-jet gravity wave activity

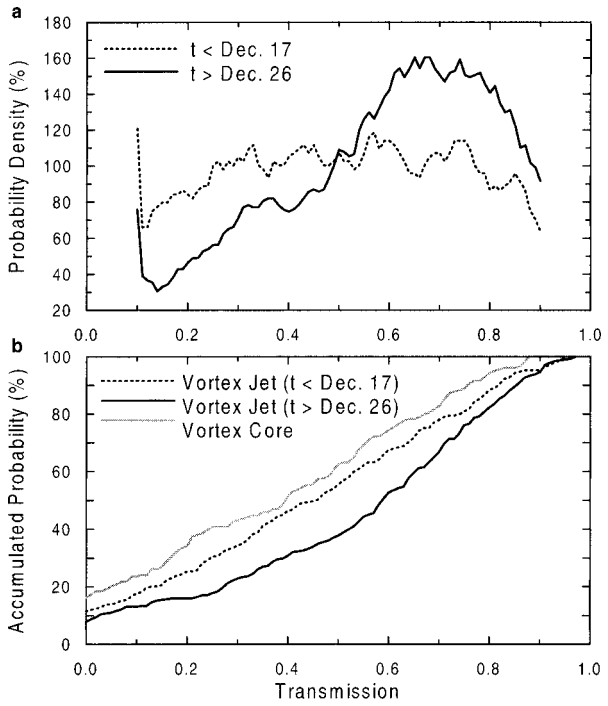

FIG. 10. (a) Histograms for vortex-jet gravity wave transmission values over Eureka during Nov–Mar of the 1992/93–1997/98 winters, each smoothed with a boxcar mean of 0.2 width. (b) The corresponding (unsmoothed) graphs of accumulated probability for the histograms given in (a). A vortex core histogram is not shown in (a) for reasons of clarity.

that was related to elevated wind speeds and enhanced wave transmission. It is of interest to contemplate how changes in gravity wave activity might affect the vortex in turn. In what follows it will be demonstrated how increases in vortex-jet gravity wave activity may drive significant warming in the vortex core. A scale-analysis calculation indicates that the late-December gravity wave activity rise should produce a warming consistent with the observations of Duck et al. (1998, 2000a).

Consider first that a rise in stratospheric gravity wave activity should result in increased momentum deposition and gravity wave drag at higher levels. The effect of increased drag in the vortex jet can be most easily diagnosed using the TEM circulation equations (Andrews and McIntyre 1976; Palmer 1981), which are formulated for zonal-symmetric flows. We use the TEM framework as a matter of convenience, and take the vortex axis to be placed at the pole. Note that in zonal-mean/planetary wave studies observations at the pole do not correspond to the axis of the ''real vortex'' because of high-latitude asymmetries during disturbance events; Duck et al. (2000b) have demonstrated that even during a stratospheric warming (where temperatures over the pole rise dramatically) the lower stratospheric temperatures in the ''real'' vortex core can remain cold.

The subset of the TEM equations required includes the zonal momentum equation

$$\partial\overline{u}/\partial t - f\overline{v}^* = \overline{F_D}, \tag{4}$$

the thermodynamic energy equation

$$\partial\overline{T}/\partial t + N^2HR^{-1}\overline{w}^* = \overline{J}/c_p, \tag{5}$$

and the mass conservation equation

$$\partial\overline{v}^*/\partial y + \rho_0^{-1}\partial(\rho_0\overline{w}^*)/\partial z = 0, \tag{6}$$

where $\overline{u}(y, z)$ is the mean zonal wind speed; $\overline{v}^*(y, z)$ and $\overline{w}^*(y, z)$ are the transformed meridional and vertical wind speeds, respectively; $\overline{T}(y, z)$ is the temperature; $f(y)$ is the Coriolis parameter; and $\overline{J}(y, z)$ is the diabatic heating rate. The drag force per unit volume $\overline{F}_D(y, z)$ is due to both large- and small-scale eddies. It is important to note that in the absence of eddies, the transformed wind speeds $\overline{v}^*$ and $\overline{w}^*$ equal the mean meridional and vertical wind speeds $\overline{v}$ and $\overline{w}$ exactly; in the presence of eddies, $\overline{v}^*$ and $\overline{w}^*$ approximate the zonal mean Lagrangian circulation. In this formulation z is a vertical coordinate defined by

$$z \equiv -H \ln(p/p_s) \tag{7}$$

for a fixed scale height

$$H = RT_c/g, \tag{8}$$

where T_c is the constant scale temperature and p is the pressure (p_s is the surface pressure). The reference density ρ_0 is defined by

$$\rho_0(z) \equiv \rho_0(0)e^{-z/H} \tag{9}$$

and the squared buoyancy frequency is

$$N^2 = (g/T_c)[d\overline{T}/dz + (\overline{T}/T_c)\Gamma], \tag{10}$$

where $\Gamma = g/c_p$ is the adiabatic lapse rate, g is the gravitational acceleration, c_p is the heat capacity of air at constant pressure, and R is the gas constant. The definition for the buoyancy frequency given in Eq. (10) is different from that in the appendix because a log-pressure vertical coordinate system is used here [Eq. (7)] rather than the geometric altitude.

The TEM circulation equations are applied to the case of increased gravity wave drag in the manner depicted in Fig. 11. Before mid-December, the vertical gravity wave momentum fluxes are small, and so the circulation is well described by a balance between the pressure gradient and Coriolis forces. However, late-December increases in vortex-jet gravity wave momentum fluxes should be expected to produce increased drag in the vortex jet at the wave breaking level. The momentum balance that results induces a small flow into the vortex core, and the ensuing mass pileup compresses the underlying air, which warms adiabaticaly. A determination of the warming magnitude is the purpose of this section.

The chief assumptions in the calculation are as follows. 1) The evolution of the gravity wave field above Eureka is representative of other locations within the High Arctic; 2) increases in stratospheric gravity wave potential energy densities result in proportional increas-

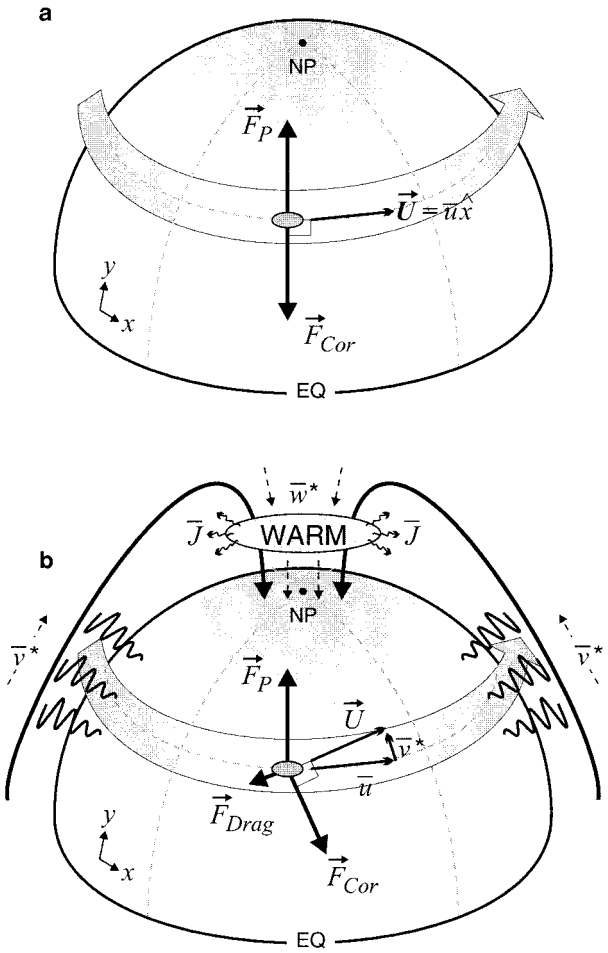

FIG. 11. (a) The Northern Hemisphere winter steady-state circulation resulting from differential solar heating only. The northward pressure gradient force $\mathbf{F}_P$ and the southward Coriolis force $\mathbf{F}_{Cor}$ balance so that the flow velocity $\mathbf{U}$ is purely zonal. The atmosphere is in radiative equilibrium and so the net diabatic heating rate $\overline{J}$ is zero everywhere. (b) The Northern Hemisphere winter steady-state circulation in the presence of eddy-induced drag. The balance of forces is now between the pressure gradient force, the Coriolis force, and the wave drag force $\mathbf{F}_{Drag}$, which leads to a small meridional velocity $\overline{v}^*$ in addition to the zonal flow $\overline{u}$. The mass piled up over the north pole (NP) compresses the underlying air, causing it to warm. In the steady state, this compressional heating is balanced by radiative cooling ($\overline{J} \neq 0$ since the temperature is away from equilibrium), and the net mass flux $\rho_0\overline{w}^*$ in the warm region is downward.

es in the gravity wave drag at the gravity wave breaking level; 3) the gravity wave breaking level begins near the stratopause; and 4) temperatures warmer than radiative equilibrium in the vortex core are forced only by gravity wave drag in the vortex jet. Surely the assumption that the gravity wave field at other locations evolves similarly to what is observed at Eureka must be verified by further observation; it does, however, seem likely when considering that the changes in gravity wave activity observed at Eureka depend strongly on the vortex evolution in general (note that we are not concerned with the absolute magnitudes of the gravity wave perturbations at each location).

The assumption that increases in stratospheric gravity wave potential energy densities result in proportional increases in the gravity wave drag at the wave breaking level is justified by considering that the vertical flux of horizontal momentum for linear waves in a nonrotating Boussinesq fluid is given by

$$\Im = k\left(\frac{E}{\omega}\right)\frac{\partial w}{\partial m},$$

where E is the total wave energy per unit volume and ω is given by Eq. (1) (Bretherton 1969). Using the dispersion relation [Eq. (2)] and substituting for ω with $c = 0$ yields

$$\Im = \frac{U}{N}k\cos\theta \cdot E$$

and so the momentum flux is equal to the wave energy multiplied by a few other terms. Because the stratospheric wind speeds increase during winter (as is shown in Fig. 8) and the buoyancy frequency N decreases due to increasing temperatures in the vortex upper stratosphere (Duck et al. 2000a), the momentum flux may actually increase above what has been assumed during the course of winter. However, due to the other uncertainties, this effect will be neglected in what follows.

Next, the assumption that gravity waves begin to break near the stratopause is supported by the rocket measurements of Lübken (1997), which show turbulence in both the upper and lower mesosphere during wintertime; the summertime data show turbulence only in the upper mesosphere. Furthermore, mountain wave calculations by Bacmeister (1993) show significant gravity wave momentum deposition in the wintertime vortex jet beginning at the stratopause. Note that gravity waves may break well below mean-flow-induced critical levels due to instability in the wave field itself (Hodges 1967; Dewan and Good 1986; Hines 1991).

The final assumption that temperatures warmer than radiative equilibrium in the vortex core are forced by gravity wave drag in the vortex jet seems appropriate from the work of Holton (1983), Hitchman et al. (1989), and Garcia and Boville (1994), who showed that the separated winter stratopause in the Arctic owes its existence to gravity wave driving; Holton (1983) achieved a warm stratopause in the vortex core without any planetary wave driving at all. Furthermore, numerical models without parameterized gravity wave drag or high enough resolution to explicitly resolve gravity waves exhibit an unrealistically cold polar winter stratosphere in the zonal mean (Hamilton 1996).

Arguments that explain why the vortex core warming observed at Eureka is not likely driven by planetary wave breaking have been given elsewhere. In brief, the measurements show that temperatures in the vortex core upper stratosphere are persistently warm regardless of

the history of large-scale stratospheric disturbance (Duck et al. 2000a). Warm vortex core temperatures are not expected from radiative considerations because of the lack of insolation at high latitudes during winter; another explanation is required. Case studies were used by Duck et al. (2000b) to demonstrate that the vortex core is positioned above Eureka in relatively undisturbed stratospheric conditions, and so a mechanism apart from planetary wave breaking is likely needed to explain vortex core warming. In quiet vortex conditions the planetary waves are usually refracted to midlatitudes where they are dissipated (Palmer 1981), whereas a high-latitude forcing is required here. Regardless, warming induced by planetary waves is usually seen in the confluent region between the vortex and Aleutian High (Fairlie and O'Neill 1988; Fairlie et al. 1990; Duck et al. 2000a,b) and not in the vortex core except during major events. Only minor stratospheric warmings occurred during the six winters considered here (Duck et al. 2000b). Finally, the vortex core warming of 1996 was sustained through the winter (Duck et al. 2000a), even though planetary wave disturbances propagating from below during February and March of that year were less than in any of the preceding 18 years (Coy et al. 1997).

Now, consider that the vortex can be treated approximately as a symmetric flow around an axis translated to the pole, so that the TEM circulation equations are applicable. In the steady state, gravity wave drag in the vortex jet must be balanced by a meridional flow (i.e., flow toward the vortex center) so that the momentum equation [Eq. (4)] becomes

$$\overline{F_D} = -f\overline{v}^*. \tag{11}$$

Substituting Eq. (11) into the mass conservation equation [Eq. (6)] and rearranging gives

$$\overline{F_D} f^{-1}(\partial \ln\overline{F_D}/\partial y - \partial \ln f/\partial y) = \rho_0^{-1}\partial(\rho_0\overline{w}^*)/\partial z \tag{12}$$

as the relation that determines the vertical descent in the vortex core corresponding to the meridional flow. The second term in parentheses on the left-hand side of Eq. (12) is much smaller than the first in our region of interest and so it will be neglected [the Coriolis force does not vary much at Arctic latitudes whereas the drag force decreases over a relatively small distance (see Bacmeister et al. 1993)]. Following similar arguments by Haynes et al. (1991), suppose that the drag force decreases over the length L in the meridional direction and the vertical mass flux $\rho_0\overline{w}_0^*$ develops in a layer of depth D, so that Eq. (12) gives

$$\overline{w}_0^* \approx \overline{F_D} D/fL \tag{13}$$

as a scale for the vertical velocity in the vortex core immediately below the gravity wave breaking altitude z_b. The length scale L can be taken as the radius of the vortex, and D as the depth of the layer within which the waves break; these parameters divide out in the calculation, and so assigning values to them now is unnecessary (the implicit assumption here is that L and D do not change as the warming develops).

Now, in the steady state the thermodynamic energy equation [Eq. (5)] implies that descent in the vortex core is accompanied by an amount of radiative cooling given by

$$(N^2H/R)\overline{w}^* = \overline{J}/c_p. \tag{14}$$

The radiative term in Eq. (14) is frequently approximated by Newtonian cooling,

$$\overline{J}/c_p = -(\overline{T} - T_r)/\tau_r, \tag{15}$$

where the air mass at temperature $\overline{T}$ cools to the equilibrium temperature T_r on a temperature dependent timescale $\tau_r(\overline{T})$. Substituting Eq. (15) into Eq. (14) and differentiating yields

$$\frac{\delta\overline{T}}{\overline{T} - T_r} = \frac{\delta N^2 H}{N^2 H} + \frac{\delta\tau_r}{\tau_r} + \frac{\delta\overline{w}^*}{\overline{w}^*}, \tag{16}$$

where δ represents a small change in any of the given variables.

The first two terms on the right-hand side of Eq. (16) can be estimated for temperature perturbations $\delta\overline{T}$ through the use of scaling arguments. The first term scales as

$$\frac{\delta N^2 H}{N^2 H} = \frac{\delta[d\overline{T}/dz + (\overline{T}/T_c)\Gamma]}{d\overline{T}/dz + (\overline{T}/T_c)\Gamma} \sim \frac{D_w^{-1} + \Gamma/T_c}{d\overline{T}/dz + \Gamma}\cdot\delta\overline{T}, \tag{17}$$

where D_w is the depth to which the warming penetrates and where $\overline{T} = T_c$ has been taken in the denominator.[1] The scaling for the second term can be determined by consulting Shine's (1987) Fig. 11, which shows that the variation of the radiative relaxation time with temperature for polar night perturbations in the upper stratosphere is approximately

$$\frac{\delta\tau_r}{\delta\overline{T}} \approx -\frac{\tau_r^2}{C}, \tag{18}$$

where $C = 1500$ K day^{-1}. The second term on the right-hand side of Eq. (16) can then be reduced to

$$\frac{\delta\tau_r}{\tau_r} \sim -\frac{\tau_r}{C}\cdot\delta\overline{T}. \tag{19}$$

A scale for the third term on the right-hand side of Eq. (16) can be found for the upper stratosphere by differentiating Eq. 13, which gives

[1] Note that by writing $\overline{T}_f = \overline{T}_i + \delta\overline{T}$, where $\overline{T}_i$ is the initial unperturbed temperature profile and $\overline{T}_f$ is the final temperature profile containing the perturbation $\delta\overline{T}$ over depth D_w, that $\delta(d\overline{T}/dz) \sim dT_f/dz - dT_i/dz = (d\overline{T}_i/dz + \delta\overline{T}/D_w) - d\overline{T}_i/dz = \delta\overline{T}/D_w$, as is employed in Eq. (17).

$$\frac{\delta \overline{w}_0^*}{\overline{w}_0^*} \sim \frac{\delta \overline{F_D}}{\overline{F_D}}. \tag{20}$$

With the scales for each term on the right-hand side of (16) determined, the change in vortex core temperatures near the stratopause due to changes in vortex-jet gravity wave drag can be estimated. Substituting Eqs. (17), (19), and (20) into Eq. (16) yields

$$\frac{\delta \overline{T}}{T_w} \approx \frac{\delta \overline{F_D}}{\overline{F_D}}, \tag{21}$$

where the warming temperature scale T_w is defined by

$$\frac{1}{T_w} = \frac{1}{\overline{T} - T_r} - \frac{D_w^{-1} + \Gamma/T_c}{d\overline{T}/dz + \Gamma} + \frac{\tau_r}{C}. \tag{22}$$

For an infinitely deep warming in an isothermal atmosphere with the radiative relaxation neglected, the warming temperature scale is given by $T_w = (\overline{T}/T_r)(\overline{T} - T_r)$, where $T_c = \overline{T}$ has been used. The radiative relaxation timescale in Eq. (22) acts to suppress warming, as would be expected since it decreases quadratically with increasing temperature in this formulation. The depth term acts to enhance warming as D_w decreases, and warming is decreased where the stratospheric temperatures increase with height.

Equation (21) [with Eq. (22)] expresses, in an extremely simple and compact form, the approximate vortex core temperature change in the upper stratosphere expected to accompany a change in gravity wave momentum deposition in the vortex jet in terms of measurable quantities. Using the mean vortex core temperature profile from Duck et al. (2000a), the parameters relating to temperature can be estimated as $T_c = 260 \pm 10$ K, $\overline{T} - T_r = 100 \pm 15$ K [T_r is taken from Shine (1987)], and $d\overline{T}/dz = 3 \pm 0.5$ K km^{-1} for the upper stratosphere. From Shine (1987), the radiative timescale in the polar night upper stratosphere is $\tau_r = 20 \pm 5$ days. The warming depth scale is likely to be within the range of a few scale heights to the depth of increasing temperatures in the stratosphere, that is, $D_w = 20 \pm 7$ km. Substituting these values into Eq. (22) gives the warming temperature scale as $T_w = 61 \pm 21$ K, where all of the uncertainties have been added in quadrature. The fractional change in gravity wave drag within the vortex jet can be estimated from the data given in Table 1 as $\delta\overline{F_D}/\overline{F_D} = 59 \pm 14\%$. The predicted warming in the upper stratosphere of the vortex core following the observed change in the gravity wave activity is therefore $\delta T = 36 \pm 14$ K.

These calculations show that a vortex core warming of a few tens of degrees should be expected to accompany the observed changes in vortex-jet gravity wave activity. The error bounds show that the calculation is only moderately sensitive to changes in the input parameters. It is desirable that a detailed model including gravity waves and a radiative transfer scheme be constructed so that the temperature changes with time at all levels can be determined with more certainty. It would also be useful to employ a three-dimensional model to evaluate the role of planetary waves.

5. Discussion and conclusions

In section 3a, it was shown that the gravity wave activity was low for measurements obtained in the vortex core, outside of the vortex altogether, and in the vortex jet before mid-December. Gravity wave energies in the vortex jet increased dramatically in late December, a change that was sustained through the end of measurements in late March. This increase is surprising because late-December increases in planetary wave activity could be expected to cause more critical-level filtering in general (Garcia and Boville 1994). The elevated amounts of high arctic gravity wave activity last only until the annual springtime vortex breakdown (Duck and Whiteway 2000).

In sections 3b and 3c, higher levels of gravity wave activity were shown to be correlated with higher stratospheric wind speeds and decreased critical-level filtering above Eureka. It was also demonstrated that wind speeds in the vortex jet increase during November and December and that critical-level filtering is much reduced after late December, and so the late-December vortex-jet gravity wave energy increases were apparently due to changes in the propagation conditions. It seems likely, however, that critical-level filtering is dependent on the strength of the stratospheric winds (i.e., the two diagnostics are inseparable): when wind speeds in the middle atmosphere are high, the vortex jet penetrates to lower altitudes thereby reducing wind turning and the amount of critical-level filtering.

That gravity wave activity is dependent upon stratospheric wind speeds and critical-level filtering is consistent with the study of Whiteway et al. (1997), although here the relationships are shown in a statistical sense. High wind speeds and low critical-level filtering do not automatically imply high gravity wave activity, but rather correspond to a distribution of gravity waves spread to higher energy values.

The observation that increased gravity wave activity is associated with the vortex jet is also consistent with the study of McLandress et al. (2000), who made a similar observation using data from the Microwave Limb Sounder (MLS) on the Upper Atmosphere Research Satellite. The MLS measures temperature variances in the horizontal whereas the lidar at Eureka obtains them in the vertical, and so these independent studies strongly support each other.

The effects of changes in gravity wave activity on the large-scale thermal structure of the stratospheric vortex were explored in section 4. The calculations there revealed that a vortex core warming on the order of several tens of degrees should accompany the increases

in gravity wave activity found in the vortex jet in late December. Consider, then, that an upper-stratospheric vortex core warming of 25 ± 2 K was observed to occur on average in late-December during the same six winters considered here (Duck et al. 1998, 2000a). The tandem development of increased gravity wave activity in the vortex jet and vortex core warming, along with the calculations performed in section 4, support the following theory: warmings in the upper stratosphere of the wintertime arctic vortex core can be forced by gravity wave drag in the vortex jet near the stratopause.

The measurements and calculations suggest the following description for the dynamic evolution of the stratospheric vortex: during November and December, temperatures in the vortex core decrease in response to radiative cooling during the dark high arctic winter months. Decreasing temperatures in the vortex core lead to a strengthening of the vortex jet. Stronger vortex winds allow the increased transmission of gravity waves that are Doppler shifted to long vertical wavelengths and so are less likely to break as they propagate through the stratosphere. When gravity waves propagating through the vortex jet dissipate near the stratopause and higher, a drag is exerted that forces flow into the vortex core. The ensuing vortex-core mass pileup near the stratopause causes a large adiabatic warming that limits the strength of the vortex jet. Equilibrium occurs on average, it seems, around the end of December. The net effect of the gravity waves is to provide a feedback loop whereby the vortex strength self-regulates.

The gravity wave feedback mechanism may have implications for studies of ozone depletion. The processes leading to the chemical destruction of ozone are highly temperature dependent; significant ozone depletions are observed in the vortex core where temperatures may drop below the chlorine activation threshold of roughly 195 K. However, a balance between radiative cooling and gravity wave driving are required to determine temperatures in the vortex core. This balance will be sensitive to the details of parameterizations used in circulation models. The incorporation of realistic gravity wave energy distributions and vortex core warming is necessary for models in any effort to predict the future state of the ozone layer and stratospheric circulation in general.

Acknowledgments. The authors wish to thank J. Bird, D. Donovan, and D. Velkov for participating in the measurement campaigns at Eureka. The temperature and height global analyses were supplied by NCEP. This work was carried out as part of the research program of the Centre for Research in Earth and Space Technology at York University. The Eureka Weather Station and stratospheric observatory are operated by the Meteorological Service of Canada. Financial support was provided by MSC and the Natural Sciences and Engineering Research Council of Canada.

APPENDIX

Gravity Wave Extraction Procedure

In order to study the gravity waves evident in measured temperature profiles quantitatively, the induced perturbations must be distinguished from the background atmospheric conditions. Gravity waves in the stratosphere typically have wavelengths that vary from a few kilometers to over 10 kilometers and have amplitudes from a few kelvins to more than 10 K, with the longer vertical wavelengths corresponding to larger wave amplitudes. The basic-state thermal structure itself varies on scales of about 30 km and greater, which adds a significant complication. A useful gravity wave extraction procedure must be able to reliably remove the background thermal structure under this wide range of conditions.

The background profile $T_0(z)$ for each 10-min average temperature profile $T(z)$ is estimated by combining a series of overlapping least squares cubic polynomials fits. Each of the fits are 25 km in length and are centered in 1.5-km intervals. In creating the average background profile, only the middle third of each fit is retained in full; the end portions (which may wag considerably) are smoothly removed from the average by decreasing their contribution exponentially with distance from the center portion (an e-folding factor of 3 km is used). The final result is smoothed with a 1.5-km boxcar mean.

The night-average fractional temperature variance $\overline{[T'(z)/T_0(z)]^2}$ is calculated from the series of 10-min average perturbation profiles given by $T'(z) = T(z) - T_0(z)$. The fractional noise variance σ_T^2 due to the uncertainty in N_P perturbation profiles is estimated as

$$[\sigma_T(z)]^2 = N_p^{-1} \sum_{i=1}^{N_P} [\delta T(z)/T_0(z)]_i^2,$$

where $\delta T(z)$ is the uncertainty in the measured temperature profile. The fractional noise variance is subtracted from the average fractional temperature variance profile to yield the gravity wave variance profile. The uncertainty in the gravity wave fractional variance profile is taken as $\sigma_T^2/\sqrt{N_P}$ (Whiteway and Carswell 1995). The potential energy per unit mass E_p for the wave field is determined by using

$$E_p = \frac{1}{2}\left(\frac{g}{N}\right)^2 \overline{\left(\frac{T'}{T_0}\right)^2},$$

where g is the acceleration due to gravity. The buoyancy frequency N is given by

$$N^2(z) = \frac{g}{T_0}\left(\frac{dT_0}{dz} + \Gamma\right),$$

where Γ is the adiabatic lapse rate g/c_p (c_p is the heat capacity of air at constant pressure). The top of the potential energy profile is taken as 2.5 km below the

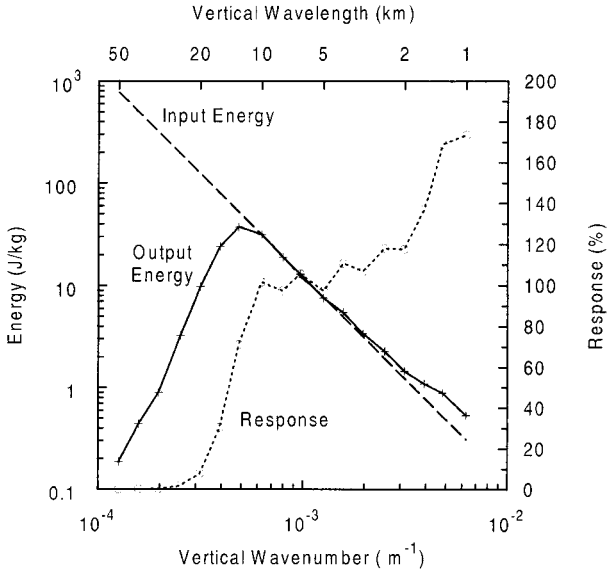

FIG. A1. A response curve for the gravity wave extraction procedure when tested on simulated lidar data. Monochromatic waves with known input energies and wavelengths (dashed line) were used to perturb simulated temperature profiles; when the waves were extracted by using a series of polynomial fits to estimate the background profile (see appendix), the output energies were obtained (solid line). The response is the ratio of output energy to input energy (dotted line). The gravity wave extraction routine is seen to extract the wave energies to within 20% for wavelengths between 2 and 15 km.

altitude where the noise variance overwhelms the gravity wave variance. Although the variance profile can extend down to the bottom of the temperature profile, only potential energy data above 30 km in altitude are considered so that no end effects due to wag in the background fits affect the analysis.

In order to test the spectral response of the gravity wave extraction procedure, several sets of 10-min integrated lidar signal profiles were simulated (30 profiles per set). The signal profiles were constructed by using a density profile from a model atmosphere (Fleming et al. 1990) and the dependence of Rayleigh lidar signal profiles $N_\gamma(z)$ on the atmospheric density $\rho(z)$,

$$N_\gamma(z) = C_n\rho(z)/z^2,$$

where z is the altitude and C_n is a normalization constant that incorporates several different instrumental parameters. The signal profiles were normalized to the number of photon counts obtained at 40 km from a 10-min integrated lidar observation on 14 February 1996 (12 235 counts). The background noise level for that night (40 shots per bin) was added to the signal (300-m resolution), as well as a measure of Gaussian distributed noise corresponding to both the signal and background levels. Each set of signal profiles was perturbed by a single propagating sinusoidal wave; a different wave energy and wavelength were used for each set of signals. The waves were scaled to reflect the range of wavelengths and amplitudes appropriate to the disturbances observed above Eureka. Temperature profiles were produced from the simulated signals and the wave variances were extracted according to the procedures outlined above. The perturbation energies were calculated and compared to the known input values in order to create the response curve shown in Fig. A1.

As is shown in Fig. A1, the gravity wave extraction procedure described here yields the correct potential energy densities to within about 20% for vertical wavelengths between 2 and 15 km. For vertical wavelengths shorter than 2 km, the input wave energies were extremely small, and so they could not be measured accurately. Vertical wavelengths larger than 25 km, corresponding to background variability, are essentially invisible to the extraction procedure and account for only energy densities of a few Joules per kilogram at most. Vertical wavelengths between 15 and 25 km correspond to the transition region from waves to background variability, and are only partly extracted by the background fitting procedure. Disturbances of this type are not usually seen by the lidar at Eureka.

REFERENCES

Andrews, D. G., and M. E. McIntyre, 1976: Planetary waves in horizontal and vertical shear: The generalized Eliassen–Palm relation and the mean zonal acceleration. *J. Atmos. Sci.,* **33,** 2031–2048.

Bacmeister, 1993: Mountain-wave drag in the stratosphere and mesosphere inferred from observed winds and a simple mountain-wave parameterization scheme. *J. Atmos. Sci.,* **50,** 377–399.

Booker, J. R., and F. P. Bretherton, 1967: The critical layer for internal gravity waves in a shear flow. *J. Fluid. Mech.,* **27,** 513–539.

Bretherton, F. P., 1966: The propagation of groups of internal gravity waves in a shear flow. *Quart. J. Roy. Meteor. Soc.,* **92,** 466–480.

——, 1969: Momentum transport by gravity waves. *Quart. J. Roy. Meteor. Soc.,* **95,** 213–243.

Carswell, A. I., A. Ulitsky, and D. I. Wardle, 1993: Lidar measurements of the arctic stratosphere. *SPIE,* **2049,** 9–23.

Coy, L., E. R. Nash, and P. A. Newman, 1997: Meteorology of the polar vortex: Spring 1997. *Geophys. Res. Lett.,* **24,** 2693–2696.

Dewan, E. M., and R. E. Good, 1986: Saturation and the ''universal'' spectrum for vertical profiles of horizontal scalar winds in the atmosphere. *J. Geophys. Res.,* **91,** 2742–2748.

Duck, T. J., 1999: High arctic observations of strato-mesospheric temperatures and gravity wave activity. Ph.D. thesis, York University, 174 pp.

——, and J. A. Whiteway, 2000: Seasonal transition in gravity wave activity during the springtime stratospheric vortex breakdown. *Geophys. Res. Lett.,* **27,** 3477–3480.

——, ——, and A. I. Carswell, 1998: Lidar observations of gravity wave activity and arctic stratospheric vortex core warming. *Geophys. Res. Lett.,* **25,** 2813–2816.

——, ——, and ——, 2000a: A detailed record of high arctic middle atmospheric temperatures. *J. Geophys. Res.,* **105,** 22 909–22 918.

——, ——, and ——, 2000b: Sudden stratospheric and stratopause warmings. Observations of temperatures in the middle atmosphere above Eureka. *Atmospheric Science across the Stratopause, Geophys. Monogr.,* No. 123, Amer. Geophys. Union, 207–212.

Dunkerton, T. J., and N. Butchart, 1984: Propagation and selective transmission of internal gravity waves in a sudden warming. *J. Atmos. Sci.,* **41,** 1443–1460.

Fairlie, T. D. A., and A. O'Neill, 1988: The stratospheric major warm-

ing of winter 1984/85: Observations and dynamical inferences. *Quart. J. Roy. Meteor. Soc.*, **114,** 557–578.
——, M. Fisher, and A. O'Neill, 1990: The development of narrow baroclinic zones and other small-scale structure in the stratosphere during simulated major warmings. *Quart. J. Roy. Meteor. Soc.*, **116,** 287–315.
Fleming, E. L., S. Chandra, J. J. Barnett, and M. Corney, 1990: Zonal mean temperature, pressure, zonal wind and geopotential height as functions of latitude. *Adv. Space Res.*, **10,** (12)11–(12)59.
Garcia, R. R., and B. A. Boville, 1994: ''Downward control'' of the mean meridional circulation and temperature distribution of the polar winter stratosphere. *J. Atmos. Sci.*, **51,** 2238–2245.
Gill, A. E., 1982: *Atmosphere–Ocean Dynamics.* Academic, 662 pp.
Hamilton, K., 1996: Comprehensive meteorological modelling of the middle atmosphere: A tutorial review. *J. Atmos. Terr. Phys.*, **58,** 1591–1628.
Hauchecorne, A., and M. L. Chanin, 1980: Density and temperature profiles obtained by lidar between 35 and 70 km. *Geophys. Res. Lett.*, **7,** 565–568.
Haynes, P. H., C. J. Marks, M. E. McIntyre, T. G. Shepherd, and K. P. Shine, 1991: On the ''downward control'' of extratropical diabatic circulations by eddy-induced mean zonal forces. *J. Atmos. Sci.*, **48,** 651–678.
Hines, C. O., 1988: A modeling of atmospheric gravity waves and wave drag generated by isotropic and anistropic terrain. *J. Atmos. Sci.*, **45,** 309–322.
——, 1991: The saturation of gravity waves in the middle atmosphere. Part II: Development of Doppler-spread theory. *J. Atmos. Sci.*, **48,** 1360–1379.
Hitchman, M. H., J. C. Gille, C. D. Rodgers, and G. Brasseur, 1989: The separated polar winter stratopause: A gravity wave driven climatological feature. *J. Atmos. Sci.*, **46,** 410–422.
Hodges, R. R., 1967: Generation of turbulence in the upper atmosphere by internal gravity waves. *J. Geophys. Res.*, **72,** 3455–3458.
Holton, J. R., 1983: The influence of gravity wave breaking on the general circulation of the middle atmosphere. *J. Atmos. Sci.*, **40,** 2497–2507.
Kanzawa, H., 1989: Warm stratopause in the Antarctic winter. *J. Atmos. Sci.*, **46,** 435–438.
Labitzke, K., 1981: Stratospheric-mesospheric midwinter disturbances: A summary of observed characteristics. *J. Geophys. Res.*, **86,** 9665–9678.
Lindzen, R. S., 1981: Turbulence and stress owing to gravity wave and tidal breakdown. *J. Geophys. Res.*, **86,** 9707–9714.
Lübken, F.-J., 1997: Seasonal variation of turbulent energy dissipation rates at high latitudes as determined by in situ measurements of neutral density fluctuations. *J. Geophys. Res.*, **102,** 13 441–13 456.
Matsuno, T., 1971: A dynamical model of the stratospheric sudden warming. *J. Atmos. Sci.*, **28,** 1479–1494.
——, 1982: A quasi one-dimensional model of the middle atmosphere circulation interacting with internal gravity waves. *J. Meteor. Soc. Japan*, **60,** 215–226.
McIntyre, M. E., and T. N. Palmer, 1983: Breaking planetary waves in the stratosphere. *Nature*, **305,** 593–600.
——, and ——, 1984: The ''surf zone'' in the stratosphere. *J. Atmos. Terr. Phys.*, **46,** 825–849.
McLandress, C., M. J. Alexander, and D. L. Wu, 2000: Microwave limb sounder observations of gravity waves in the stratosphere: A climatology and interpretation. *J. Geophys. Res.*, **105,** 11 947–11 967.
Palmer, T. N., 1981: Diagnostic study of a wavenumber-2 stratospheric sudden warming in a transformed Eulerian-mean formalism. *J. Atmos. Sci.*, **38,** 844–855.
Sato, K., T. Kumakura, and M. Takahashi, 1999: Gravity waves appearing in a high-resolution GCM simulation. *J. Atmos. Sci.*, **56,** 1005–1018.
Schoeberl, M. R., 1978: Stratospheric warmings: Observations and theory. *Revs. Geophys. Space Phys.*, **16,** 521–538.
Shine, K. P., 1987: The middle atmosphere in the absence of dynamical heat fluxes. *Quart. J. Roy. Meteor. Soc.*, **113,** 603–633.
Sica, R. J., and M. D. Thorsley, 1996: Measurements of superadiabatic lapse rates in the middle atmosphere. *Geophys. Res. Lett.*, **23,** 2797–2800.
Whiteway, J. A., and A. I. Carswell, 1994: Rayleigh lidar observations of thermal structure and gravity wave activity in the High Arctic during a stratospheric warming, *J. Atmos. Sci.*, **51,** 3122–3136.
——, and ——, 1995: Lidar observations of gravity wave activity in the upper stratosphere over Toronto. *J. Geophys. Res.*, **100,** 14 113–14 124.
——, and T. J. Duck, 1996: Evidence for critical level filtering of atmospheric gravity waves. *Geophys. Res. Lett.*, **23,** 145–148.
——, and ——, 1999: Enhanced arctic stratospheric gravity wave activity above a tropospheric jet. *Geophys. Res. Lett.*, **26,** 2453–2456.
——, ——, D. P. Donovan, J. C. Bird, S. R. Pal, and A. I. Carswell, 1997: Measurements of gravity wave activity within and around the arctic stratospheric vortex. *Geophys. Res. Lett.*, **24,** 1387–1390.
Yoshiki, M., and K. Sato, 2000: A statistical study of gravity waves in the polar regions based on operational radiosonde data. *J. Geophys. Res.*, **105,** 17 995–18 011.